

A feasibility study of biodegradable magnesium-aluminum-zinc-calcium-manganese (AZXM) alloys for tracheal stent application

Jingyao Wu, Boeun Lee, Partha Saha and Prashant N Kumta 

Abstract

Airway obstruction conditions are relatively rarely observed in clinical settings but nevertheless, extremely challenging to handle, especially when observed in pediatric patients. Several surgical procedures, including tracheal resection, end-to-end tracheal anastomosis, and tracheoplasty, have been developed and practised of late, to treat airway obstruction. However, the clinical outcome is typically not satisfactory due to airway restenosis conditions that develop following surgery. Various types of stents are currently available for airway stenting ranging from non-degradable silicone tubes and bio-inert metallic stents (bare or coated with polymer matrix) to hybrid silicone tubes strengthened by metallic cores, but none of the stents provides the satisfactory long-term effectiveness. Therefore, there is a significant clinical need for a biodegradable airway stent that would maintain airway patency and totally degrade over time after meeting the desired objectives. The present study aims to investigate biodegradable magnesium-aluminum-zinc-calcium-manganese (AZXM) alloy as a potential tracheal stent. The new AZXM alloy was fabricated by partially replacing aluminum in commercial AZ31 alloy with calcium. The present study demonstrates that calcium preferentially segregates along the grain boundaries as intermetallic phases (Mg_2Ca) and is homogeneously distributed in the magnesium matrix. The extruded AZXM alloy showed less pitting, higher corrosion resistance in Hank's Balanced Salt Solution (HBSS) compared to the as-cast and solution-treated AZXM alloys and exhibited optimized mechanical properties. In vitro cytotoxicity evaluation using human trachea epithelial cells demonstrated excellent cyto-compatibility of AZXM alloys compared to pure Mg and commercial AZ31 validated by a very preliminary rabbit in vivo tracheal model study. Preliminary results show that the approach to use biodegradable AZXM alloys as a tracheal stent is indeed promising, although further alloy processing is required to improve the ductility needed followed by a more exhaustive in vivo study to demonstrate full viability for stent applications.

Keywords

Magnesium alloy, biodegradable, tracheal stents, cyto-compatibility, airway

Introduction

Airway obstruction is a relatively rare occurrence in the clinic but could be very challenging to handle, especially when observed in pediatric patients. Airway obstruction could be caused by various reasons, such as trauma, long-term intubation, and cancer. In the case of pediatric patients, congenital tracheomalacia and tracheal stenosis are the most common reasons.¹ Several surgical procedures, including tracheal resection, end-to-end tracheal anastomosis, and tracheoplasty, have been developed to treat airway obstruction.^{2,3} However, the clinical outcome employing these techniques is not satisfactory due to the development of airway restenosis following surgery. Therapeutic endoscopic-based technologies, such as

laser resection and stenting, could reduce the need of high-risk open surgery and provide immediate relief.⁴ Airway stenting is a valuable adjunct to the other therapeutic bronchoscopic techniques as stenting provides mechanical support to maintain the patency of airway lumen and therefore, secures long-term effectiveness.

Department of Bioengineering, Swanson School of Engineering, University of Pittsburgh, Pittsburgh, USA

Corresponding author:

Prashant N Kumta, Department of Bioengineering, Swanson School of Engineering, University of Pittsburgh, 815C Benedum Hall, 3700 O'Hara Street, Pittsburgh, PA 15261, USA.

Email: pkumta@pitt.edu

Various types of stents are available for airway stenting ranging from silicone tubes and metallic stents (bare or coated with polymer matrix) to hybrid silicone tubes strengthened by metallic cores. The decision to select a certain type of stent is decided based on the individual clinical symptoms. However, even though all these stents exhibit efficient short-term palliation, none of the stents provides satisfactory long-term effectiveness. Non-degradable silicone tubes interfere with the mucociliary clearance⁵ while bio-inert and also non-degradable metallic stents provide better mechanical support and mucociliary clearance albeit causing tissue ingrowth and severe granulation formation.⁶ Because of these severe complications, secondary surgical procedures are often needed for removal of the stents. These surgeries may be difficult to perform while exposing the patient to additional risks. Due to the obvious deficiencies of currently available stents, there is a significant clinical need for a biodegradable airway stents that would maintain airway patency and totally degrade overtime after fulfilling the desired objectives.

Over the past decade, magnesium and magnesium alloys have emerged as novel biodegradable metallic materials. As biocompatible metals, magnesium-based alloys provide better mechanical support compared to conventional polymer and ceramic materials. At the same time, due to the biodegradable nature, magnesium alloy-based implants need not to be implanted permanently in patients and will dissolve overtime obviating the need for secondary retrieval surgeries. Magnesium is the second most abundant intracellular element and the fourth most abundant element in the body, while also performing multiple essential physiological functions in the human body.⁷ Therefore, the release of Mg ions with the degradation of Mg alloy-based implants has shown various bioactive effects on specific cell and tissues.^{8–10} For example, studies have revealed that magnesium-based alloys have shown osteo-inductive function rendering them useful for orthopedic applications.¹¹ However, to the best of our knowledge, there are no previous publications to date reported, on the use of magnesium stents for intraluminal tracheal stent application.

In this paper, we report the evaluation and feasibility of newly developed AZXM alloy for airway stenting application. The specific AZXM alloy was fabricated into rods using conventional melting and casting followed by extrusion. The mechanical properties, in vitro degradation behavior, and cyto-biocompatibility of the AZXM alloys were subsequently evaluated. In addition, a short-term pilot implantation study of the prototype stents employing a simple tubular design demonstrated initial feasibility for evaluating the airway tissue response to AZXM alloys. Results of these studies are described in the various sections of this manuscript.

Materials and methods

Materials fabrication and characterization

AZXM alloy was prepared by the conventional melting and casting route. Pure metal ingots or pellets were added in the sequence of Mg, Mn, Al, Ca, and Zn based on the nominal composition and were melted in a mild steel crucible at 720°C using an electrical resistance furnace (Wencesco Inc., Chicago, IL). Ar + 0.1% SF₆ was used to create a protective environment. The melt was kept at 720°C for 10 min for homogenization, and the elements were mixed by appropriate stirring and then poured into a mild steel mold pre-heated at 500°C. The as-cast ingots were solution treated (T4 treated) at 385°C for 10 h under ultra-high purity (UHP) argon atmosphere in a tubular furnace and then quenched in water. After T4 treatment, the ingots were machined into cylinders ($\phi = 38 \text{ mm} \times 60 \text{ mm}$) and extruded into rods ($\phi = 12 \text{ mm}$) at 300°C with an extrusion speed of 1 mm/s followed by quenching in water. The extrusion ratio used was 10 for all the ingots. The actual chemical composition of AZXM alloy was determined by inductively coupled plasma optical emission spectroscopy (ICP-OES, iCAP duo 6500 Thermo Fisher, Waltham, MA). The structure and phase purity of the alloys were analyzed by XRD (Philips X'Pert PRO diffractometer), employing CuK α ($\lambda = 1.54056 \text{ \AA}$) radiation with an Si detector (X'celerator). The X-ray generator was operated at 45 kV and 40 mA at a 2θ range of 10–80°.

Microstructure characterization

To observe the microstructure of AZXM alloys, round plate samples ($\phi = 10 \text{ mm} \times 2 \text{ mm}$) were sliced by the lathe from the center of the as-cast/T4-treated ingots and the extruded rods. All the samples were grinded with SiC abrasive sandpapers up to 1200 grit and polished with monocrystalline diamond suspension spray (1 μm , Buehler) and finally with Masterprep[®] Alumina Suspension (0.05 μm , Buehler). Polished samples with mirror-like finish were etched in acetic picral solution (5 ml acetic acid, 6 g picric acid, 10 ml water, and 100 ml ethanol) for 5–10 s. The microstructure of the samples were captured using a Nikon Optiphot microscope (Nikon, Tokyo, Japan) and scanning electron microscope (SEM; JSM6610LV, JEOL) coupled to an energy dispersive X-ray (EDX) (Oxford Instruments, Abingdon, Oxfordshire, UK).

Mechanical property characterization

Tensile tests were performed for the as-cast, T4-treated and extruded AZXM alloys as well as commercially obtained AZ31 alloys used as the reference. The tensile bars were machined along the long axis of the ingots or

extruded rods by computer numerical control (CNC) machine. The size of the tensile bars was determined as per the ASTM E8/E8M-11 standard to be 12.7 mm gauge length and 3 mm × 3 mm gauge area. For each sample, a stress–strain curve was generated by Instron 5969 testing system (Instron, Norwood, MA) equipped with an extensometer (Instron 2630 series, Norwood, MA) measuring the elongation. Three typical stress–strain curves obtained from each group were used to calculate the yield strength (YS), ultimate tensile strength (UTS), and percent elongation at fracture (EL) using the Bluehill® three Testing Software for Mechanical Testing Systems (Instron, Norwood, MA). The average and standard deviation were calculated for all the three samples for each group.

In vitro degradation evaluation

Immersion test was conducted to evaluate the *in vitro* degradation of AZXM alloys based on the ASTM standard G31-12a. Round plate samples ($\phi = 10$ mm × 2 mm) were sliced by lathe from the center of the as-cast/T4-treated ingots or extruded rods along the long axis. All the samples were ground with SiC abrasive sandpapers up to 1200 grit. Following grinding, the samples were sonicated in ethanol, weighed and sterilized under ultraviolet (UV). Each sample was subsequently immersed in Hank's Balanced Salt Solution (HBSS) in a 50 ml bio-reaction centrifuge tube with a 0.22 μ m hydrophobic membrane in the vent cap. The ratio of HBSS volume to sample surface area is 0.20 ml/mm². All the samples were stored in CO₂ incubator and kept in 37°C and 5% CO₂ humidified atmosphere. After immersion for one, two, and three weeks, the samples were retrieved from buffer media, washed in DI water, ethanol, and dried in air. The corrosion products were removed by immersion in solution of 200 g chromium trioxide, 10 g silver nitrate, and 100 ml water for 10 min. The samples were then washed in DI water, ethanol, dried in air and weighed. The corrosion rate was calculated based on the mass loss using the equation listed below:

$$\text{Corrosion rate (mm/year)} = (K \times W) / (A \times T \times D) \quad (1)$$

where the constant K is 3.65×10^3 , W is mass loss (g), A is the surface area of each sample (cm²), T is the immersion time (day), and D is the density of each alloy (g/cm³). One sample from each group at each time point was mounted in epoxy to obtain the cross-section profile of degradation layer and degradation morphology.

In vitro cyto-compatibility test

Extract preparation. Round plate samples ($\phi = 10$ mm × 2 mm) were sliced and ground with SiC abrasive sandpapers up to 1200 grit. All the samples were then ultrasonically cleaned in ethanol, dried in air, sterilized under UV for 30 min each side. The extract was obtained based on the IOS 10993-12-2012 standard. All the samples were pre-incubated in bronchial epithelial cell growth medium (BEGM™; Lonza, Walkersville, MD, USA) for 72 h at 37°C in a humidified atmosphere with 5% CO₂. The ratio of the sample surface area to medium volume is 1.25 cm²/ml. After pre-incubation, the extract was filtered with 0.22 μ m syringe-driven filter and kept in 4°C freezer. In total, three samples were used for each group at each time point for conducting the following tests described below. The concentrations of different elements in the extract were measured by ICP-OES.

Cell viability test. Normal human bronchial epithelial cells (BEAS-2B, American Type Culture Collection, Rockville, MD) were cultured in BEGM medium at 37°C in a humidified atmosphere with 5% CO₂ before seeded into 96-well plates at the density of $8 \times 10^3/100$ μ l in each well. After incubation for 24 h to allow the cells to attach the 96-well plates, the media were replaced by the extract diluted by BEGM at different dilution ratios (10%, 25%, 50%, and 75%). The same volume of BEGM medium was added as control. BEAS-2B cells were incubated in the extract for another one or three days. CyQUANT® NF Cell Proliferation Assay Kit (Life Technologies, Grand Island, NY) was used following the described protocol. Briefly, before the test, a standard curve was generated by measuring the fluorescence intensities of 4×10^3 , 8×10^3 , 1.2×10^4 , and 1.6×10^4 BEAS-2B cells. After each time point, BEAS-2B cells in 96-well plates were washed with phosphate buffer solution (PBS) and then incubated with 50 μ l dye binding solution. The plates were incubated at 37°C and measured using the fluorescence microplate reader with excitation at ~485 nm and emission detection at ~530 nm. The highest fluorescence intensity value was picked and converted to cell number using the standard curve.

Live and dead and DAPI/ α -actin staining. BEAS-2B cells (1.6×10^4) were seeded in each well of 48-well plates and incubated for 24 h for analyzing cell attachment. The cell culture medium was then replaced by a mixture of 50% alloy extract and 50% BEGM. After three days of incubation, the BEAS-2B cells were stained with calcein and ethidium homodimer-1 using commercially available LIVE/DEAD® Viability/Cytotoxicity Kit (Invitrogen Inc., Karlsruhe, Germany). The cells were

then captured under fluorescence with excitation/emission ~ 495 nm/ ~ 515 nm (live cells) and excitation/emission ~ 495 nm/ ~ 635 nm (dead cells), respectively. To image the cell morphology, the BEAS-2B cells were accordingly stained by DAPI (AppliChem, Darmstadt, Germany) and Phalloidin (Sigma-Aldrich, St. Louis, MO) to correspondingly visualize the nucleus and F-actin, respectively.

In vivo evaluation of AZXM prototype stents. To obtain a preliminary feasibility assessment of biocompatibility of the AZXM alloys, the prototype stents were machined from the extruded AZXM rods using the CNC machining. The stents were designed as a non-expandable simple tube structure with an outer diameter of 5 mm, inner diameter of 4 mm, and length of 15 mm, respectively. All the stents were sonicated in isopropanol for 5 min and dried in air and then terminally sterilized with γ -irradiation (J L Shepherd, San Fernando, CA) before implantation. The dose rate is 2425 cGy/min and the total dosage is 2,000,000 cGy.

The animal study was conducted under a protocol approved by the Institutional Animal Care and Use Committee (IACUC) at the University of Pittsburgh. One rabbit was anesthetized by intramuscular injection of ketamine/xylazine, 35 mg/kg and 5 mg/kg, respectively, before surgery. A vertical midline incision was made to expose the airway. The prototype stent was delivered through the incision and placed inside the tracheal lumen. The anterior vertical airway incision was closed using 4/0 Vicryl (polyglactin 910) and the skin and subcutaneous layer were together subsequently closed with 4/0 Vicryl (polyglactin 910) interrupted sutures allowing air.

After four weeks of implantation, endoscopy imaging was performed before the rabbit was anesthetized. The laryngo-tracheal region of the airways was then harvested with the prototype stent remaining inside and fixed in formalin. The tissue was trimmed and embedded in paraffin. The embedded paraffin blocks were then fixed on a microtome and cut into thin slices and stained with hematoxylin–eosin for histological analysis.

Statistics

The obtained results were expressed as the mean \pm standard deviation. Two-way ANOVA was

conducted to determine the differences between different groups of samples. Statistical significance was defined as $p < 0.05$. Statistical analysis was performed with the IBM SPSS Statistics 24 for Windows.

Results and discussion

Microstructure and mechanical properties of AZXM alloy

AZ31 alloy is normally explored as a biodegradable magnesium alloy in numerous studies because of the high corrosion resistance and mechanical properties.^{12–14} Aluminum (Al) is the most commonly used alloying element which improves the mechanical properties and corrosion resistance of magnesium alloys.¹⁵ However, the neurotoxicity of Al is extremely well-known and has been reported in previous publications.^{16–18} The release of Al ions as the magnesium alloy degrades over time might lead to neurotoxicity issues similar to what has been reported.^{16–18} Therefore, it would be prudent and beneficial to reduce the content of Al and maintain the mechanical properties and corrosion resistance similar to AZ31 alloys. In this study, a novel AZXM alloy was thus developed by modifying the commercial AZ31 alloy composition by reducing the Al content from 3 wt.% to 2 wt.% with corresponding introduction of calcium (Ca). Ca was incorporated to lower the Al content and reduce the cytotoxicity based on previous studies.^{19,20}

Table 1 lists the actual chemical composition of the AZXM alloy. The actual elemental content of each alloy was determined to be close to the nominal composition of the AZXM alloy for all the elements with the exception of Mn. The reasons for this deviation in Mn content could be: (1) Mn has a much higher melting temperature compared to other elements in the AZXM alloy. It is therefore, likely that Mn is not fully melted; (2) In the Mg–Al alloy, Mn is known to react with iron, a likely detrimental impurity to form $Al_5(Fe, Mn)_2$ which precipitates at the bottom of the melt.²¹ As a result, it is likely that the actual amount of Mn in the generated alloy is lower than the intended nominal composition. This deviation, however, did not adversely influence the results of the study as described and discussed later.

As shown in Figure 1(a), the as-cast AZXM alloy consists of fine equiaxed grains with secondary phase precipitation homogeneously distributed within the

Table 1. Chemical composition of AZXM alloy.

	Al	Zn	Ca	Mn	Mg
Nominal composition (wt.%)	2%	1%	0.6%	0.2%	Bal.
Chemical composition (wt.%)	1.92%	1.05%	0.56%	0.02%	Bal.

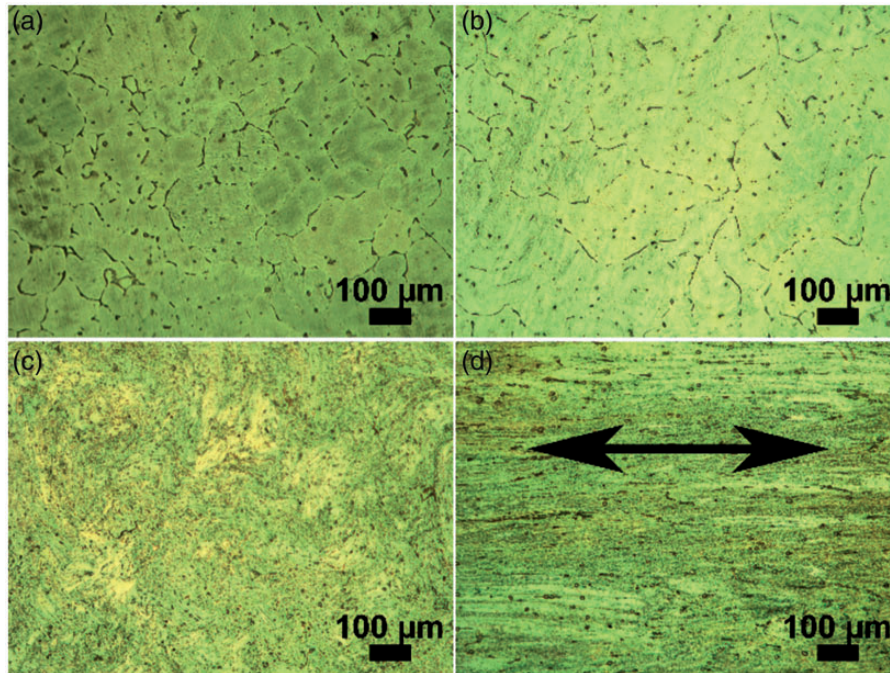


Figure 1. Optical microstructure of the AZXM alloys (a) as-cast, (b) T4 treated and extruded, (c) transverse direction, and (d) longitudinal direction; the arrow indicates the extrusion direction.

grains. The average grain size is $169 \pm 35 \mu\text{m}$. After T4 treatment, the AZXM alloy exhibited no significant change but there was partial dissolution and reprecipitation of the second phase along the grain boundaries (Figure 1(b)). The grain size slightly increased to $182 \pm 2 \mu\text{m}$. Extruded AZXM alloys (Figure 1(c) and (d)) exhibited the typical fibrous extrusion texture. The grains are significantly refined and elongated due to the severe plastic deformation associated with the extrusion phenomena occurring along the extrusion direction indicating the occurrence of dynamic recrystallization of grains during the extrusion process. Similar results were observed in the SEM/EDX analysis (Figure 2). The SEM image showed microstructural features similar to what was observed under the optical microscope. The enlarged view of the microstructure of AZXM alloys and elemental analysis of the grain and grain boundaries by SEM and EDX analyses are shown in Figure 2(b), (d), (f), (g). The EDX (Figure 2 (g)) results indicate that the Ca content was rich in both the grain boundary and in the precipitated secondary phases. As expected, the content of Ca in the AZXM alloy in the matrix was much lower. This result is in agreement with previous studies describing that Ca is preferentially present as precipitates (Mg_2Ca) along the grain boundaries and in the second phase of magnesium alloys.^{20,22} The solubility of Ca in the Mg matrix is low with a maximal solubility of $\sim 1.35\%$ (wt.%) at 516.5°C . As the ingot cools down, a eutectic structure is thus formed between Mg_2Ca and Mg according to Mg–

Ca binary phase diagram. Therefore, Ca will preferentially concentrate in the intermetallic phases and grain boundaries. However, the XRD pattern (Figure 3) of the AZXM alloys did not reveal any obvious peaks associated with second phases, but only peaks of α -phase is seen probably due to the low volume percentage of the secondary phases formed. However, the XRD pattern of extruded AZXM ingot shows a strong Bragg's reflection along the (100) plane at $\sim 32^\circ 2\theta$ value suggesting the preferential orientation (texture) of the grains following extrusion.

For application in stents, the tensile properties are of prime importance. The tensile properties of the AZXM alloys generated are correspondingly shown in Figure 4. The as-cast AZXM alloys possessed low strength and ductility when compared to commercially obtained AZ31 alloy. T4 treatment resulted in a slight decrease in the YS. However, there was a slight improvement in the UTS. The mechanical properties significantly improved following hot extrusion. Both the strength (YS and UTS) and ductility (percent elongation to failure (EL)) of the extruded AZXM alloy were significantly improved compared to the as-cast and T4-treated AZXM alloys. Compared to commercial AZ31 alloys with YS of $165.45 \pm 8.01 \text{ MPa}$ and UTS of $259.97 \pm 7.30 \text{ MPa}$, the extruded AZXM alloys exhibited higher strengths with YS of $233.53 \pm 4.15 \text{ MPa}$ and UTS of $283.08 \pm 1.72 \text{ MPa}$. The AZXM alloy generated in this study, however, was relatively brittle compared to the AZ31 alloys. After extrusion, the AZXM

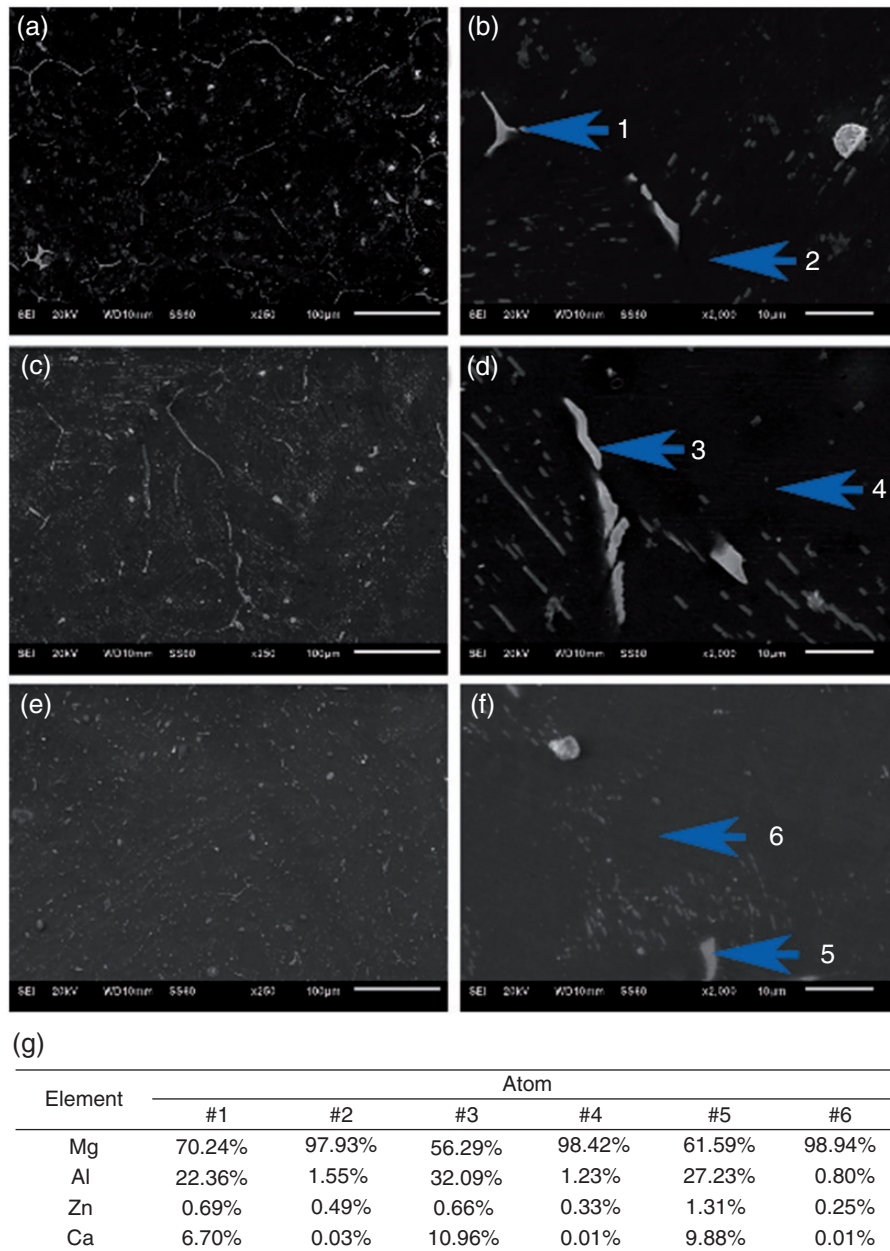


Figure 2. SEM microstructure of the AZXM alloys as-cast (a, b), T4 treated (c, d), as extruded (e, f). (g) The chemical compositions of corresponding spots obtained from EDX analysis.

alloy exhibited an elongation of $8.56 \pm 2.05\%$ at fracture, which is much lower than $17.12 \pm 1.77\%$ displayed by the AZ31 alloys. These results are in line with the previous reported observations of Mg alloys containing Ca.^{20,23}

The introduction of Ca into the Mg–Al–Zn alloy system improves the strength of the alloy owing to solid solution strengthening. The reduction in ductility after addition of Ca is also reported in the study of other Mg alloys.^{23,24} It was reported that the lamellar Mg₂Ca Laves phase has a deleterious effect on the ductility of binary Mg–Ca alloy.²⁵ The Mg₂Ca Laves phase

which is concentrated at the grain boundaries acts as the crack nucleation site. The Mg alloys are easily amenable to hot working though, similar to all metallic systems, the lower melting point of Mg further contributing to this amenability. In addition, a reduction in Al content from 3 wt.% to 2 wt.% contributes to the lower measured mechanical properties and percent elongation of the AZXM alloy. Thus, with further materials processing and alloy modifications leading to a better homogenization and improved solubility of the alloying elements, minimizing the precipitate formation and segregation, it is possible to potentially

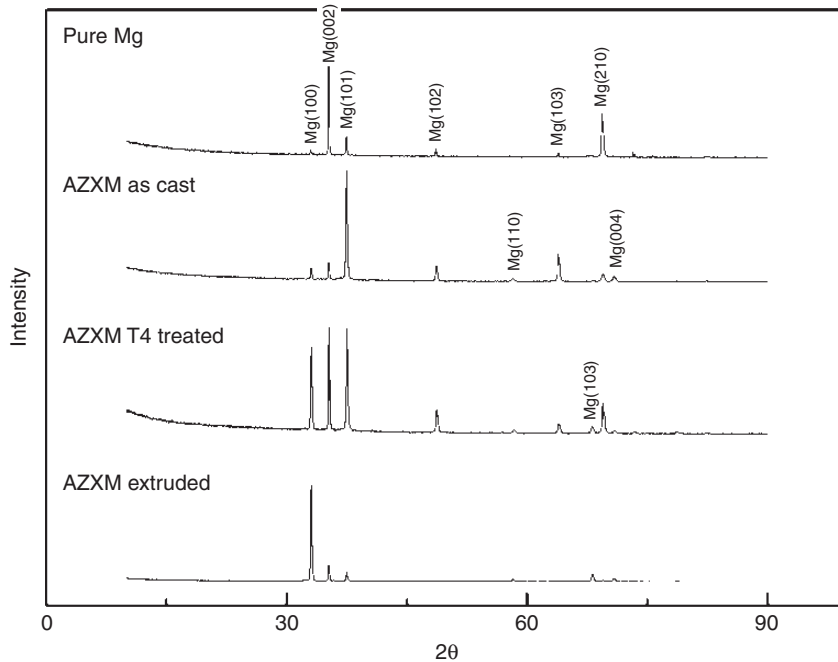


Figure 3. XRD patterns collected on the as-cast, T4-treated and extruded AZXM alloys developed in this work.

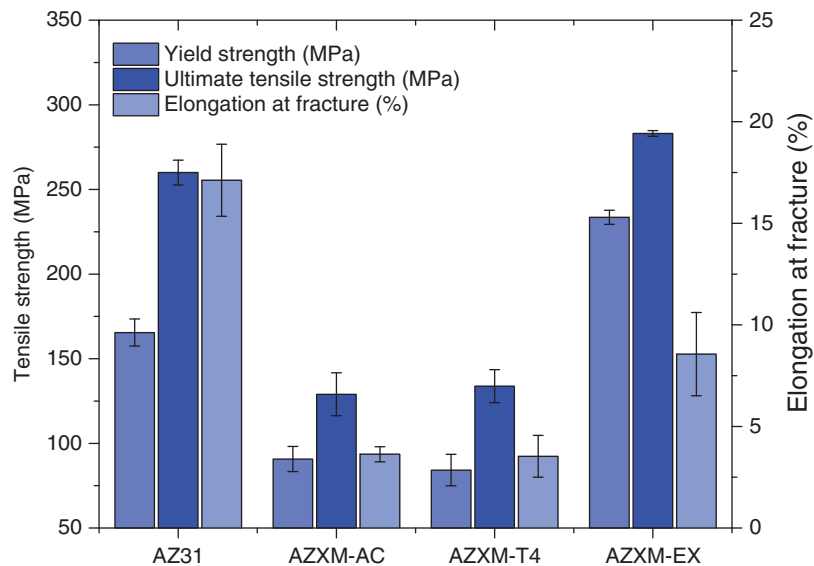


Figure 4. Mechanical properties of the AZXM alloys subjected to different conditions compared with AZ31.

improve the ductility of the AZXM Mg alloys. The use of equal channel angular processing, for example, could likely contribute towards improving the microstructure and homogeneity in order to achieve higher ductility in these alloys.

In vitro degradation of AZXM alloy

The *in vitro* degradation profile of the AZXM alloy is presented in Figure 5. The as-cast AZXM alloy group

exhibited poor corrosion resistance and demonstrated the highest corrosion rate amongst all groups. The corrosion rate was observed to increase over three weeks of immersion reaching 6.78 ± 0.31 mm/year at week 3. The AZXM alloy upon subjecting to T4 treatment displayed significantly improved corrosion resistance and the average corrosion rate peaked after two weeks of immersion (1.46 ± 0.07 mm/year), subsequently observed to decrease thereafter with a corrosion rate of 0.77 ± 0.32 mm/year at the end of three weeks. The

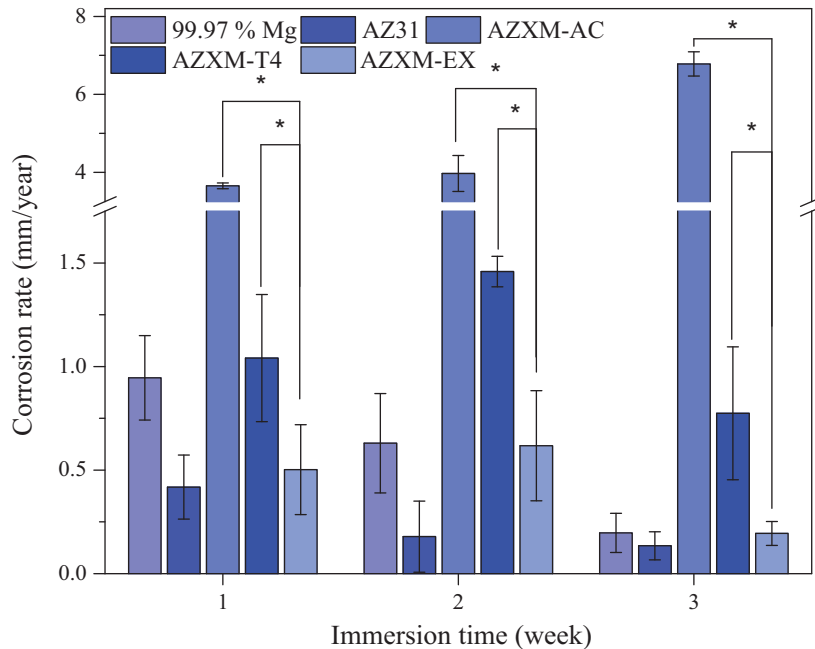


Figure 5. In vitro degradation rate of AZXM alloy in HBSS.

slowest corrosion rate of the AZXM alloy was observed after extrusion. The three-week average corrosion rate of AZXM alloy is 0.19 ± 0.06 mm/year, slightly higher than the three-week average corrosion rate of the commercially obtained AZ31 alloy (0.13 ± 0.07 mm/year).

To investigate the corrosion mode of the AZXM alloys, the cross-sections of the samples after three weeks of immersion were observed under SEM (Figure 6). Even though pure Mg exhibited relatively slow corrosion, pitting corrosion appears to be the primary mode of corrosion. The corrosion of AZ31 is much more uniform compared to pure Mg although the corrosion is not homogeneous, with pitting corrosion again being the major mode of corrosion. The as-cast AZXM, and T4-treated AZXM corrode much faster, and hence after three weeks of immersion, a thick degradation layer was formed on the surface of the samples. Compared to AZ31, even though the corrosion rate of the extruded AZXM is slightly higher, the overall corrosion appears to be more uniform (Figure 6). The EDX elemental mapping of the degradation layer for the as-cast AZXM alloy is shown in Figure 7. The result shows that the degradation layer is comprised of MgO and $Mg(OH)_2$ with Ca and P deposited on the surface of the corrosion layer.

According to previous publications, the corrosion resistance of Mg alloy can be enhanced by increasing the Ca content, although the corrosion tends to increase with the amount of Ca reaching a certain limit. Wan et al. demonstrated that $Mg-0.6Ca$

showed the highest polarization resistance with the corrosion resistance and polarization resistance decreasing when more Ca is added.²⁶ The increased corrosion rate could be explained by the presence of higher amount of the second phase that causes micro-galvanic corrosion. The enhancement of corrosion resistance after adding small amount of Ca (<1%) generally could lead to reduced oxidation in the molten condition due to the presence of lower Ca containing α -Mg activity.²³ Grain refinement also significantly improved the corrosion resistance of the AZXM alloys in this study. Ca is believed to serve as a grain refinement additive,²⁷ and extrusion further reduced the grain size leading to higher corrosion resistance. Similar results were also shown in the previous study of Mg–Ca alloy.²⁰ In this study, AZ31 showed the slowest corrosion rate indicating that replacing Al with Ca, however, leads to the presence of secondary precipitates as discussed above, causing an increase in the corrosion rate.

The corrosion of AZXM alloy is also governed by the oxide film formed on the surface of the magnesium alloy. The protective film on magnesium formed in HBSS was composed mainly of $Mg(OH)_2$. However, the $Mg(OH)_2$ layer is soluble in most aqueous environments, and incompletely covers the metal surface with localized corrosion usually occurring at the unprotected locations on the surface. The in vitro corrosion showed that, after extrusion, AZXM alloys exhibited much more uniform corrosion compared to AZ31. The reason could be that the addition of Ca stabilized the degradation layer of AZXM alloys and further inhibits

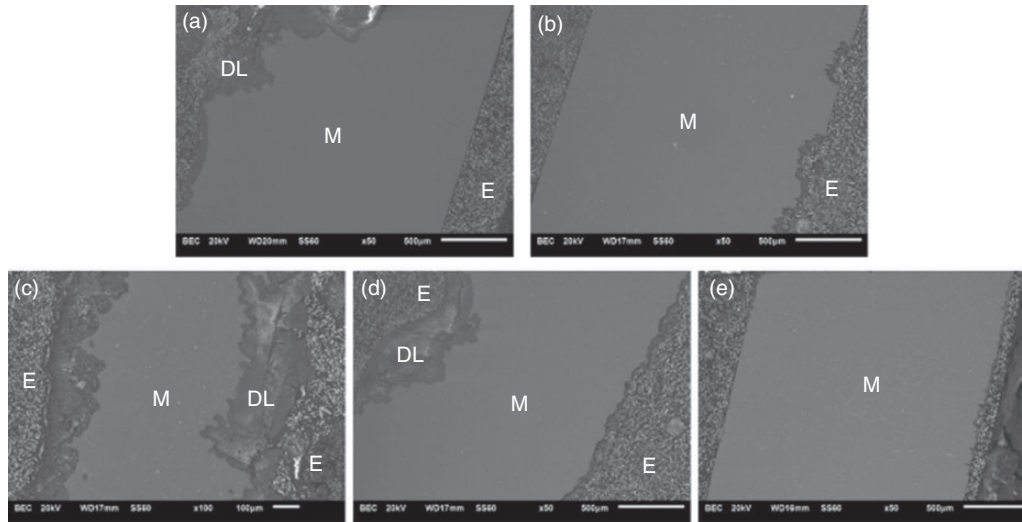


Figure 6. SEM micrographs of the corrosion profile after immersion for three weeks: (a) 99.97% pure Mg, (b) AZ31, (c) AZXM as-cast, (d) AZXM T4 treated, (e) AZXM as extruded. (E=epoxy, DL=degradation layer, M=Mg or Mg alloys.) The bar equals 500 μm for (a), (b), (d), (e) and 100 μm for (c).

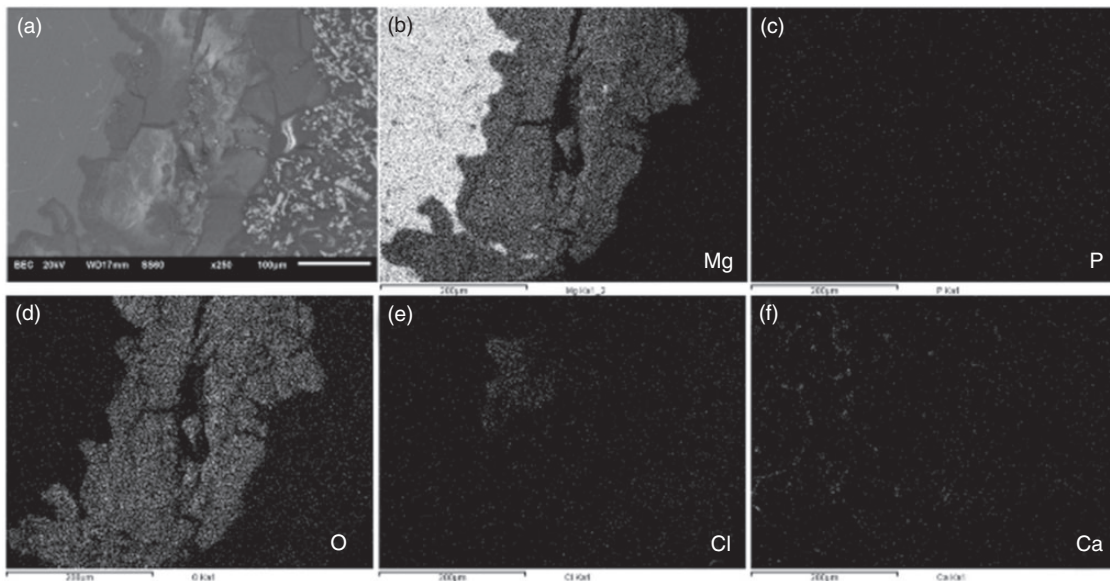


Figure 7. EDX mapping of the corrosion pit for the as-cast AZXM sample (a) SEM image of the corrosion pit; EDX mapping of (b) Mg, (c) P, (d) O, (e) Cl, (f) Ca. (The white areas in (b) to (f) are the locations where the corresponding elements were detected.)

pitting corrosion. For stent application, reduced pit formation and consequent pitting corrosion could prevent the stents from fracture and failure.

In vitro and in vivo evaluation of AZXM alloy

Figure 8(a) shows the ion concentrations of Mg, Al, Zn, and Ca in the extract as well as the elements present in BEGM. The results show that Al, Zn, and Ca are all present in the normal BEGM. Compared to the cell

culture medium, the concentration of Mg increased from ~ 12 ppm in BEGM to ~ 1000 – 1300 ppm in the extract. The concentration of Al increased slightly, implying that most of the Al is incorporated into the oxide film on the magnesium alloy surface. The Zn concentration increased in all groups except for pure Mg which indicates that the increase in Mg concentration induces the deposition of Zn on the samples. For Ca, the pure Mg and AZ31 groups both showed a dramatic drop in the Ca concentration indicating the

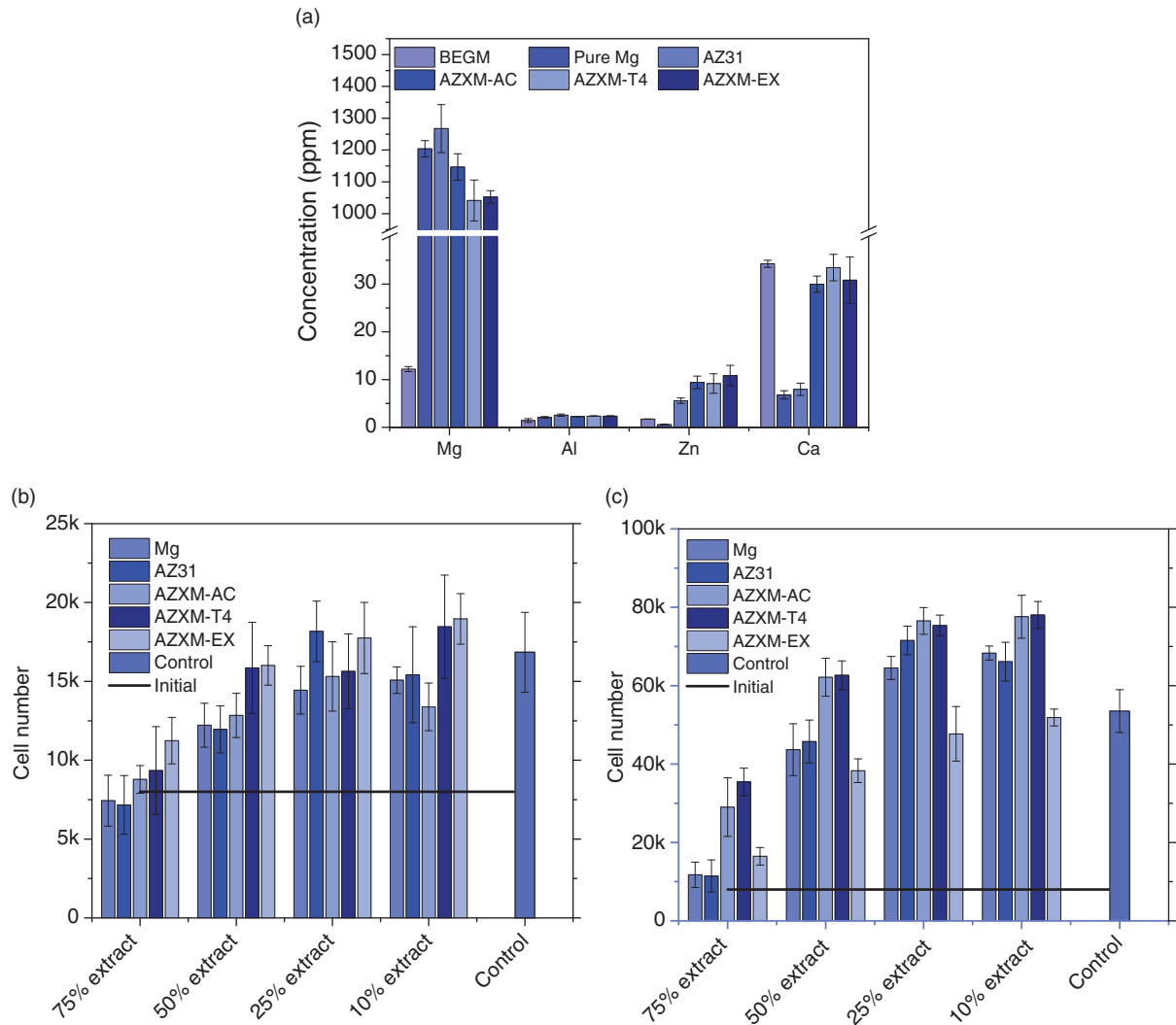


Figure 8. (a) The concentration of metal ions in extract; cell viability of BEAS-2B cultured in extracts with different dilution ratios (b) day 1, (c) day 3 (initial: number of cells initially seeded; control: number of cells after culture in normal BEGM). Control: the number of cells cultured on tissue culture plate using normal cell culture medium. Initial: the initial cell number seeded in all the experimental groups and the control group.

reduced solubility of Ca in high magnesium concentration medium. However, owing to the corrosion of AZXM, the amount of Ca released compensates the deposition of Ca, and hence the concentration of Ca in the AZXM groups remains at levels similar to the cell culture medium.

Figure 8(b) and (c) shows the cytotoxicity results of AZXM alloys performed using the BEAS-2B cells, and the CyQuant assay. The level of cytotoxicity level is evaluated by calculating the numbers of BEAS-2B cells after culture in the different concentration of the extracts for one day and three days. After one day of culture, all groups showed higher cell numbers compared to the initial cell numbers seeded (8000 cells) except for pure Mg and AZ31 75% extract groups. As the extract was diluted from 75% to 10%, the cell

number increased for most groups. After three days of culture, the cell numbers increased by 10 folds of the cell numbers initially seeded for 50% and 25% extract groups. It should be noted that, for 75% extract groups, even though the number of BEAS-2B cells was much lower compared to 10% extract groups, the number of cells still significantly increased reaching $\sim 11,000$ cells for pure Mg and AZ31 groups compared to the initial seeded cell number of 8000 cells. For AZXM alloy groups, much more cells were observed in the as-cast and T4-treated AZXM alloy groups compared to the extruded AZXM alloy group, even though the composition of the extract did not show much difference. The as-cast and T4-treated AZXM alloys showed excellent cyto-compatibility with human trachea epithelial cells. Even though the cells were

cultured in high concentration of extract (75%), the cell numbers still increased after three days of cell culture. With higher extract dilution, a higher cell proliferation was observed. It is worth noticing that for the extruded AZXM alloys, the cell proliferation was similar to the control group and lower than the as-cast and T4-treated groups. However, the ICP data of key elements in the extract showed non-significant difference between the different groups, implying that the concentration of metal ions might not be the only reason affecting the cell viability and proliferation. There may be other reasons such as the changes in the protein in the cell culture medium which could also likely affect the *in vitro* cytotoxicity result.

These studies are warranted and will be part of future studies in this system.

Similar trend was observed in the indirect live and dead cell test (Figure 9(a)). After culture in 50% extract for three days, the BEAS-2B cells in the control group appeared to aggregate showing the highest cell density. The AZXM alloy groups also demonstrated comparable live cell density compared to pure Mg and AZ31 with only few apoptotic cells observed. Figure 9 shows that the morphology of the BEAS-2B cells is normal in all the groups. Cytoskeletons of BEAS-2B cells after immersion for three days in 50% extract are shown in Figure 9(b). The BEAS-2B cells in the control groups aggregated and therefore, it is difficult to ascertain and

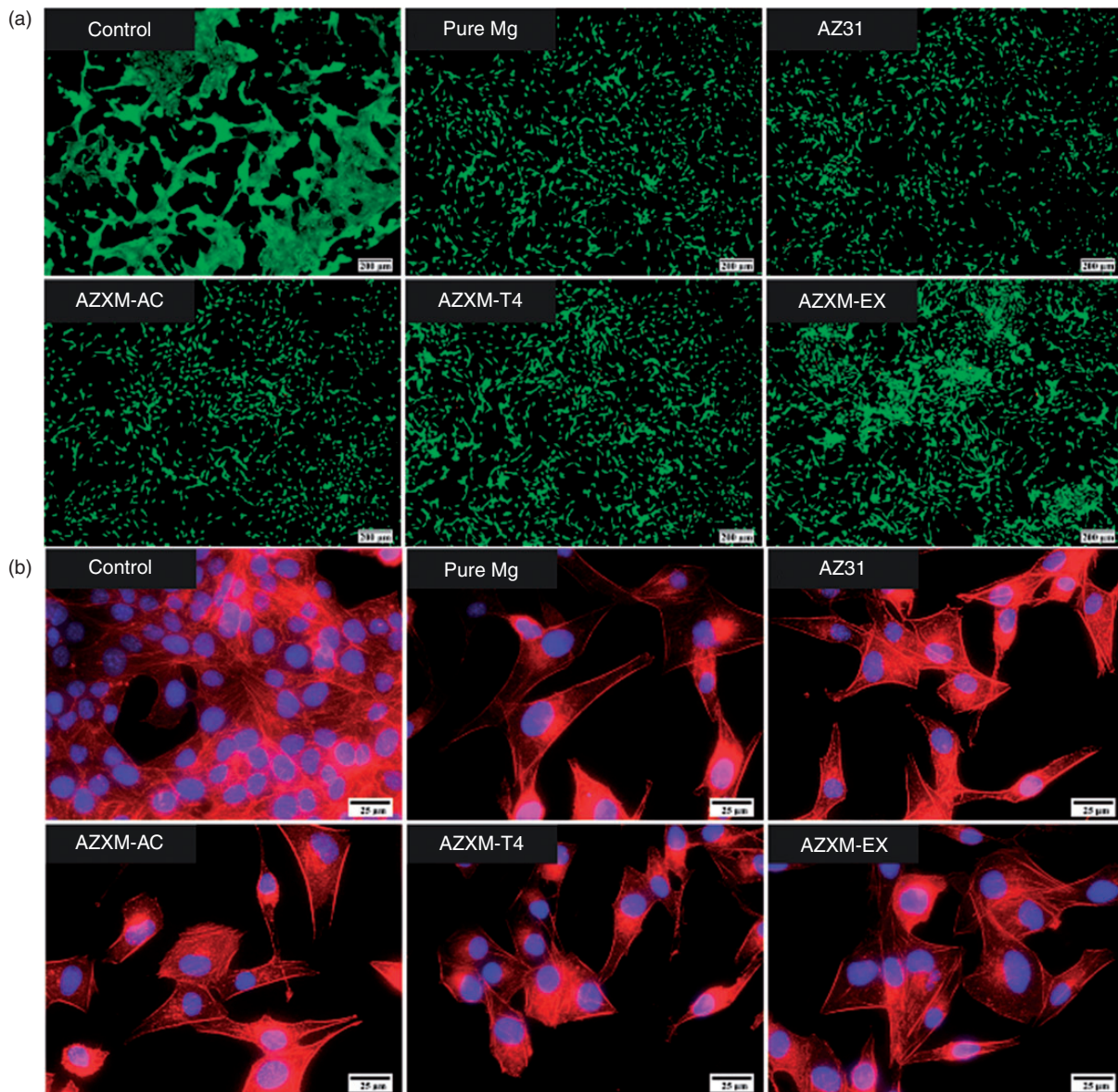


Figure 9. (a) Live and dead (scale bar = 200 μm) and (b) DAPI/F-actin staining of BEAS-2B cells after three days of culture in 50% extract of pure Mg, AZ31, and AZXM alloys (scale bar = 25 μm).

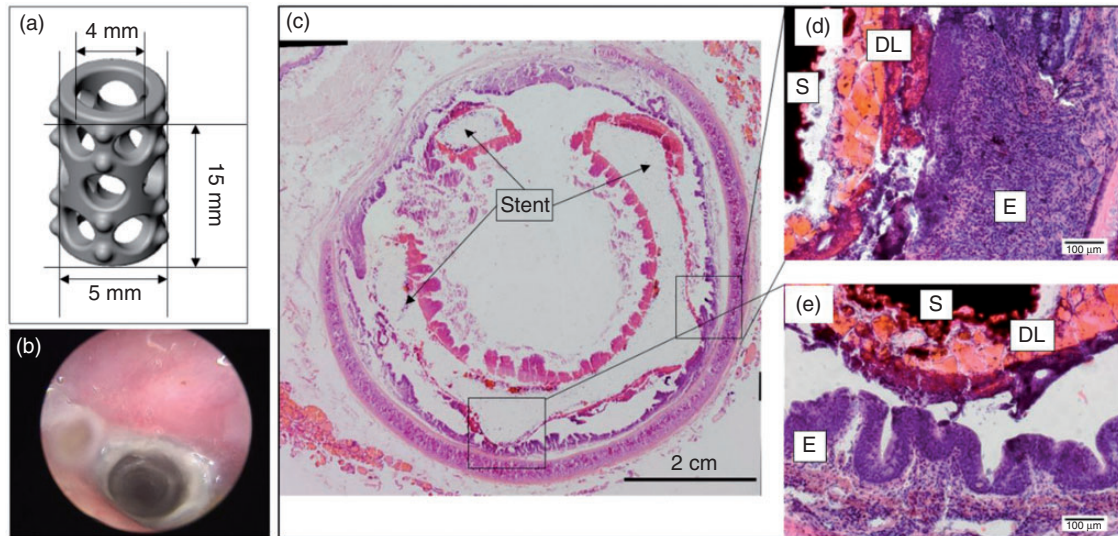


Figure 10. (a) Design of prototype AZXM stent, (b) digital endoscopy image showing stented airway after four weeks of implantation. (c)–(e) H&E staining of stented tracheal tissue following four weeks of implantation (S: stent, E: epithelium and DL: degradation layer).

distinguish clearly, the individual cell morphology. The BEAS-2B cells in all the experimental groups exhibited similar spreading and filopodia extension.

Due to the lack of any reported previous *in vivo* study on magnesium stents for tracheal stent application and to ascertain a preliminary *in vivo* response, we only implanted one AZXM prototype stent owing to the budget constraints primarily to evaluate the feasibility of the concept. The goal was not to do a thorough study to obtain a statistically relevant result. The primary aim was to ascertain if the system merits a more detailed study. The *in vivo* study presented here therefore, is only assessed to this extent and no further assessment, evaluations, and conclusions have been drawn. The stent was machined based on the design shown in Figure 10 (a). The endoscopy images indicated that a white colored gel was formed inside of the trachea as shown in Figure 10(b). The white colored gel is most likely, a mixture of mucous and fibrosis tissue. However, the airway maintained patency throughout the four-week study, and the rabbits did not exhibit any respiratory issues. H&E staining was also performed to investigate the airway tissue response. As shown in Figure 10(c) to (e), the integrity of the epithelium was maintained along the airway lumen indicating that the existence of the AZXM prototype stents did not interfere with the normal function of the tracheal epithelial layer. A thin degradation layer was formed between the epithelium and the remaining AZXM metal substrate. The normal morphology of the epithelium layers in the H&E staining images (Figure 10(d) and (e)), however, shows that the degradation layer was well tolerated by

the airway tissue. Although this is the result obtained from only one animal, the lack of any adverse reaction indeed indicates that the alloy certainly merits a more detailed study for unequivocally assessing the favorable potential in a statistically relevant rabbit tracheal model. Subsequent publications will report the results of these studies which are planned for in the near future.

Conclusions

The AZXM alloys were developed by partially replacing Al with Ca. The novel AZXM alloys accordingly exhibited higher strength compared to AZ31 alloys. The Ca preferentially segregated along the grain boundaries as secondary intermetallic phase (Mg_2Ca) and homogeneously distributed in the magnesium matrix. However, the corrosion rate of AZXM was not affected by the Mg_2Ca second phase following extrusion. The extruded AZXM alloy showed less pitting, higher corrosion resistance, and optimized mechanical properties. *In vitro* cytotoxicity evaluation using the human trachea epithelial cells also demonstrated excellent cyto-compatibility of AZXM alloys compared to pure Mg and AZ31. The as-cast and T4-treated AZXM alloys showed the highest cell numbers after three days of cell culture. Pilot implantation studies of the AZXM prototype stents showed the feasibility of the concept alloy, although more detailed studies are clearly warranted. The four-week pilot study nevertheless indicated that the airway tissue well tolerated the AZXM alloy and its degradation product. The existence of the AZXM stent also did not interfere with the

epithelium and the morphology of the epithelium was observed to be normal. Further study should focus on processing of the AZXM alloy to increase the ductility and evaluating the prototype device in relevant animal models for longer time points to demonstrate the statistical relevance and validity. It can be concluded based on the studies presented herein however, that the newly developed AZXM alloy is indeed a feasible candidate for biodegradable tracheal stent applications.

Declaration of Conflicting Interests

The author(s) declared no potential conflicts of interest with respect to the research, authorship, and/or publication of this article.

Funding

The author(s) disclosed receipt of the following financial support for the research, authorship, and/ or publication of this article: The authors would like to acknowledge the financial assistance of NSF-ERC (Grant No. EEC-0812348) for supporting this work. The authors also acknowledge the financial support of the Swanson School of Engineering, University of Pittsburgh, while Prashant N Kumta acknowledges the Edward R. Weidlein Chair Professorship and the Center for Complex Engineered Multifunctional Materials (CCEMM) for partial support of this research.

ORCID iD

Prashant N Kumta  <http://orcid.org/0000-0003-1227-1249>

References

1. Leung L, Chung PH, Wong KK, et al. Management of tracheobronchial obstruction in infants using metallic stents: long-term outcome. *Pediatr Surg Int* 2015; 3: 249–254.
2. Backer CL and Holinger LD. A history of pediatric tracheal surgery. *World J Pediatr Congenit Heart Surg* 2010; 1: 344–363.
3. Grillo HC. Development of tracheal surgery: a historical review. Part 1: techniques of tracheal surgery. *Ann Thorac Surg* 2003; 75: 610–619.
4. Bolliger CT, Sutedja TG, Strausz J, et al. Therapeutic bronchoscopy with immediate effect: laser, electrocautery, argon plasma coagulation and stents. *Eur Respir J* 2006; 27: 1258–1271.
5. Chin CS, Litle V, Yun J, et al. Airway stents. *Ann Thorac Surg* 2008; 85: S792–S796.
6. Saito Y and Imamura H. Airway stenting. *Surg Today* 2005; 35: 265–270.
7. Swaminathan R. Magnesium metabolism and its disorders. *Clin Biochem Rev* 2003; 24: 47–66.
8. Feyerabend F, Witte F, Kammal M, et al. Unphysiologically high magnesium concentrations support chondrocyte proliferation and redifferentiation. *Tissue Eng* 2006; 12: 3545–3556.
9. Zhai Z, Qu X, Li H, et al. The effect of metallic magnesium degradation products on osteoclast-induced osteolysis and attenuation of NF- κ B and NFATc1 signaling. *Biomaterials* 2014; 35: 6299–6310.
10. Dou Y, Li N, Zheng Y, et al. Effects of fluctuant magnesium concentration on phenotype of the primary chondrocytes. *J Biomed Mater Res Part A* 2014; 102: 4455–4463.
11. Witte F, Ulrich H, Palm C, et al. Biodegradable magnesium scaffolds: Part II: peri-implant bone remodeling. *J Biomed Mater Res* 2007; 81A: 757–765.
12. Zhang Y, Kent D, Wang G, et al. The cold-rolling behaviour of AZ31 tubes for fabrication of biodegradable stents. *J Mech Behav Biomed Mater* 2014; 39: 292–303.
13. Willbold E, Kaya AA, Kaya RA, et al. Corrosion of magnesium alloy AZ31 screws is dependent on the implantation site. *Mater Sci Eng B* 2011; 176: 1835–1840.
14. Yan TT, Tan LL, Xiong DS, et al. Fluoride treatment and in vitro corrosion behavior of an AZ31B magnesium alloy. *Mater Sci Eng C* 2010; 30: 740–748.
15. Gusieva K, Davies CHJ, Scully JR, et al. Corrosion of magnesium alloys: the role of alloying. *Int Mater Rev* 2015; 60: 169–194.
16. Shaw CA and Tomljenovic L. Aluminum in the central nervous system (CNS): toxicity in humans and animals, vaccine adjuvants, and autoimmunity. *Immunol Res* 2013; 56: 304–316.
17. Ebina Y, Okada S, Hamazaki S, et al. Liver, kidney, and central nervous system toxicity of aluminum given intraperitoneally to rats: a multiple-dose subchronic study using aluminum nitrilotriacetate. *Toxicol Appl Pharmacol* 1984; 75: 211–218.
18. Kawahara M. Effects of aluminum on the nervous system and its possible link with neurodegenerative diseases. *J Alzheimers Dis* 2005; 8: 171–182. discussion 209–115.
19. Kannan MB and Raman RKS. In vitro degradation and mechanical integrity of calcium-containing magnesium alloys in modified-simulated body fluid. *Biomaterials* 2008; 29: 2306–2314.
20. Li Z, Gu X, Lou S, et al. The development of binary Mg-Ca alloys for use as biodegradable materials within bone. *Biomaterials* 2008; 29: 1329–1344.
21. Friedrich HE and Mordike BL. *Magnesium technology: metallurgy, design data, automotive applications*. Germany: Springer Berlin Heidelberg, 2006.
22. Zhou Y-L, Li Y, Luo D-M, et al. Microstructures, mechanical properties and in vitro corrosion behaviour of biodegradable Mg-Zr-Ca alloys. *J Mater Sci* 2013; 48: 1632–1639.
23. Aghion E and Levy G. The effect of Ca on the in vitro corrosion performance of biodegradable Mg-Nd-Y-Zr alloy. *J Mater Sci* 2010; 45: 3096–3101.
24. Zhang E and Yang L. Microstructure, mechanical properties and bio-corrosion properties of Mg-Zn-Mn-Ca

- alloy for biomedical application. *Mater Sci Eng* 2008; 497: 111–118.
25. Chino Y, Kobata M, Iwasaki H, et al. Tensile properties from room temperature to 673 K of Mg-0.9 mass%Ca alloy containing lamella Mg₂Ca. *Mater Trans* 2002; 43: 2643–2646.
26. Wan Y, Xiong G, Luo H, et al. Preparation and characterization of a new biomedical magnesium–calcium alloy. *Mater Des* 2008; 29: 2034–2037.
27. St John DH, Qian M, Easton MA, et al. Grain refinement of magnesium alloys. *Metall and Mat Trans A* 2005; 36: 1669–1679.